Earth and Planetary Science Letters 618 (2023) 118277

Contents lists available at ScienceDirect

Earth and Planetary Science Letters

journal homepage: www.elsevier.com/locate/epsl

Absolute stress levels in models of low-heat faults: Links to geophysical observables and differences for crack-like ruptures and self-healing pulses

Valère Lambert [a,*], Nadia Lapusta [b,c]

[a] Department of Earth and Marine Sciences, University of California, Santa Cruz, CA, USA
[b] Seismological Laboratory, California Institute of Technology, Pasadena, CA, USA
[c] Department of Mechanical and Civil Engineering, California Institute of Technology, Pasadena, CA, USA

ARTICLE INFO

Article history:
Received 19 December 2022
Received in revised form 4 May 2023
Accepted 12 June 2023
Available online 28 June 2023
Editor: R. Bendick

Dataset link: https://data.caltech.edu/records/1619

Dataset link: https://data.caltech.edu/records/1620

Keywords:
fault stress
earthquake ruptures
enhanced dynamic weakening
self-healing pulse
crack-like rupture
undershoot

ABSTRACT

Absolute levels of stress on faults have profound implications for earthquake physics and fault mechanics. A number of observations suggest that well-developed, mature faults such as the San Andreas Fault are generally "weak," i.e. operate at much lower levels of shear stress compared to the higher expected shear resistance ~100 MPa at seismogenic depths. In particular, low heat flow measurements suggest shear stress levels of ~10 MPa or less on highly localized faults. Geodynamic constraints based on topography and similar considerations also support "weak" fault operation, and are comparable with heat-based constraints for some mature faults, but potentially higher for regions with substantial topography. Here, we investigate measures of average fault shear stress and their relationship to geophysically inferable quantities using numerical simulations of earthquake sequences on rate-and-state faults with low heat production, due to chronic fluid overpressure and/or enhanced dynamic weakening from the thermal pressurization of pore fluids. We review the earthquake energy balance, focusing on energy-based definitions of average shear stress and how the average fault prestress (a measure of fault strength plausibly relevant to geodynamic constraints) can be expressed as the sum of the dissipation-based average rupture stress (which can, in principle, be inferred from shear-heating constraints), and seismologically inferable source properties, such as the static stress drop and apparent stress. Our modeling demonstrates that rapid dynamic weakening and healing of shear resistance during ruptures, as exhibited in self-healing pulses, allows faults to maintain higher average interseismic stress levels despite low dynamic resistance and realistic static stress drops, providing a physical explanation for potential differences between topography-based and heat-based constraints on fault shear stress. In our models, the difference is related to stress undershoot and apparent stress, which can be as large as 1-3 times the static stress drop based on our simulations. Yet suitably large values of apparent stress (and hence radiated energy) are rarely inferred for natural earthquakes, either because radiated energy is underestimated, or suggesting that most large earthquakes do not propagate as sharp enough self-healing pulses with sufficiently large undershoot. Our results emphasize the distinction between dynamic versus static stress changes when relating earthquake source observations to absolute levels of fault stress and suggest that reviewing estimates of radiated energy and static stress drop from large earthquakes, with input from finite-fault numerical modeling, may improve constraints on absolute fault stress levels.

© 2023 The Author(s). Published by Elsevier B.V. This is an open access article under the CC BY license (http://creativecommons.org/licenses/by/4.0/).

1. Introduction

Assessing the absolute levels of stress on faults is a topic of many geological and geophysical investigations, with substantial implications for fault mechanics, earthquake physics, and geodynamics. Some of the most notable constraints on the shear stress state of mature faults, of ~20 MPa or less, are based on measurements indicating a lack of substantial heat flow around mature faults (e.g Brune et al., 1969; Lachenbruch and Sass, 1980; Tanikawa and Shimamoto, 2009; Fulton et al., 2013; Gao and Wang, 2014) and the existence of long-lived narrow shear zones that do not exhibit evidence of melting (Sibson, 1975; Rice, 2006; Chester and Chester, 1998; Wibberley and Shimamoto, 2003). Thermal measurements surrounding mature faults are in principle re-

* Corresponding author.
E-mail address: valerelambert@ucsc.edu (V. Lambert).

https://doi.org/10.1016/j.epsl.2023.118277
0012-821X/© 2023 The Author(s). Published by Elsevier B.V. This is an open access article under the CC BY license (http://creativecommons.org/licenses/by/4.0/).

lated to the average shear stress associated with shear heating during substantial fault motion. Such observations can thus provide constraints for the average dynamic shear resistance at seismic slip rates during large earthquakes. Studies of exhumed mature faults suggest that shear motion can be accommodated within narrow layers, less than one to several millimeters wide (e.g. Chester and Chester, 1998; Wibberley and Shimamoto, 2003). In order to avoid pervasive melt production during dynamic rupture, upper bounds for the average shear stress associated with shear heating are expected to be on the order of 10 MPa or less for shear localized between 1 to 10 mm (Lachenbruch and Sass, 1980; Rice, 2006; Lambert et al., 2021b). Such low shear stress values during fast slip on mature faults are supported by in-situ temperature measurements soon after major earthquake events (Tanikawa and Shimamoto, 2009; Fulton et al., 2013). Further evidence for the similarly low-stress operation of mature faults arise from inferences of steep angles between the principal stress direction and fault trace (Townend and Zoback, 2004) and the geometry of thrust-belt wedges and their internal faults (Suppe, 2007; Dielforder, 2017).

Several studies have estimated the absolute stress levels along major plate boundary faults, such as the San Andreas Fault system, by considering the force balance of tectonic block motion, topography and mantle buoyancy (Fialko et al., 2005; Fay and Humphreys, 2006; Luttrell and Smith-Konter, 2017), inferring shear stress levels of 20 to 30 MPa averaged over seismogenic depths. Similar studies suggest that the topography associated with most subduction and collisional megathrusts can be maintained by average shear stresses ranging from 7 to 25 MPa (Lamb, 2006; Luttrell et al., 2011; Dielforder, 2017; Dielforder et al., 2020), which are largely consistent with constraints based on heat flow and other shear heating considerations for these regions below 20-30 MPa (e.g. Gao and Wang, 2014). Some calculations suggest that regions with more substantial topography, such as the North Chilean subduction zone and portions of the San Andreas and San Jacinto fault zones, may require average shear stresses up to 40 MPa (Lamb, 2006; Fay and Humphreys, 2006).

All these estimates are much lower than the expected seismogenic-depth-averaged shear resistance of about 100-200 MPa, given typical quasi-static friction measurements of 0.6-0.8 in the lab and confining conditions assuming hydrostatic fluid pressures (Byerlee, 1978). However, some of the higher topography-based estimates of average fault shear stress (20-40 MPa) may also be higher than estimates from shear heating, particularly if heat-based constraints limit average shear stresses to around 10 MPa or less for faults with highly localized shear, as evidenced along some mature strike-slip faults such as the San Andreas Fault (e.g. Brune et al., 1969; Lachenbruch and Sass, 1980; Rice, 2006; Lambert et al., 2021a). Note that evidence for low-stress, low-heat operation predominantly pertains to mature plate boundary faults, whereas a number of studies suggest that less mature active faults may operate at stress levels consistent with Byerlee values of friction and hydrostatic pore pressures (Byerlee, 1978; Townend and Zoback, 2000).

In this work, we study average shear stress levels in two types of models of low-stress, low-heat mature faults based on field observations and laboratory experiments, with a focus on the relationship between averaged shear stress quantities relevant to heat-based and topography or geodynamic-based constraints. In the first model, the fault is persistently weak due to the presence of anomalously low quasi-static friction coefficients and/or low effective confinement from pervasive fluid overpressure (e.g. Brown et al., 2003; Lockner et al., 2011). In the second model, the shear resistance at seismic slip rates is significantly lower than the quasi-static shear resistance on faults during periods of slow aseismic slip and interseismic locking with negligible motion, due to enhanced dynamic weakening at seismic slip rates (e.g. Tsutsumi and Shimamoto, 1997; Rice, 2006; Tullis, 2007; Di Toro et al., 2011).

Recent numerical simulations of earthquake ruptures in these two types of fault models have demonstrated that they can be potentially distinguished by seismological observations (Lambert et al., 2021b). Earthquake ruptures in persistently weak fault models with typically inferred static stress drops (i.e. the difference in average fault shear stress before and after the earthquake) between 1 to 10 MPa (e.g. Shearer et al., 2006; Allmann and Shearer, 2009; Ye et al., 2016) propagate as crack-like ruptures. In such ruptures, seismic slip at each fault location, once initiated, continues until arrest waves arrive from the edges of the fault or other heterogeneities in the problem; as a result, the portion of the fault that slips at a given time during rupture is comparable to the final rupture size and the local slip duration at different points is comparable to the total rupture duration (Fig. 1A). The word “crack” in the name refers to analogy with opening cracks that also typically continue to open until the crack arrests at a barrier. In contrast, ruptures in quasi-statically strong, dynamically weak fault models with 1 to 10 MPa static stress drops typically propagate as self-healing pulses (e.g. Heaton, 1990; Noda et al., 2009), in which slip spontaneously arrests behind the rupture front due to rapid local weakening and then healing; as a result, only a small portion of the fault slips at a given time and the local slip duration is short relative to the rupture duration (Fig. 1B).

Numerical simulations show that self-healing pulse-like ruptures have much higher radiated energy than crack-like ruptures with the same seismic moment, average static stress drop, and average slip (Lambert et al., 2021b). This finding implies that the two types of low-stress, low-heat models can be distinguished based on the radiated energy per seismic moment of the resulting earthquake ruptures, which is proportional to the apparent stress (McGarr, 1999; Beeler et al., 2003). Persistently weak models with crack-like ruptures result in the radiated energy per moment comparable to teleseismic estimates from large megathrust earthquakes, while quasi-statically strong, dynamically weak fault models with self-healing pulses produce radiated energy per moment which is much larger than typical teleseismic estimates for large megathrust earthquakes, yet comparable to limited regional estimates from large crustal earthquakes (Ye et al., 2016; Choy and Boatwright, 1995; Perez-Campos and Beroza, 2001). The substantial difference in radiated energy results from difference in rupture dynamics and shear stress variations on the fault, as discussed further in section 4. Specifically, increasingly sharper self-healing pulses have increasingly larger stress undershoot.

Here, we consider the implications of the qualitatively different rupture dynamics between crack-like ruptures and self-healing pulses for average fault stresses. Further, we consider the link between fault stresses to seismological and other observables using energy balance considerations, building on prior work. To examine average shear stress quantities in numerical fault models consistent with the inferred low-heat, low-stress operation of mature faults, we use numerical simulations of sequences of earthquakes and aseismic slip (SEAS) on rate-and-state faults with different levels of chronic fluid overpressure and enhanced dynamic weakening due to the thermal pressurization of pore fluids (section 2.1). We perform simulations with sets of parameters based on prior studies that reproduce the typical stress drops of 1-10 MPa and comply with the heat-generation constraints. In section 2.2, we use our simulations to review previously identified conceptual differences in shear-stress evolution between the simulated ruptures of differing rupture style, crack-like vs. pulse-like. In section 3, we recall the earthquake energy budget, focusing on the energy-based definition of average shear stress and review how the average fault prestress can be expressed as the sum of the dissipation-based average rupture stress (which can, in principle,

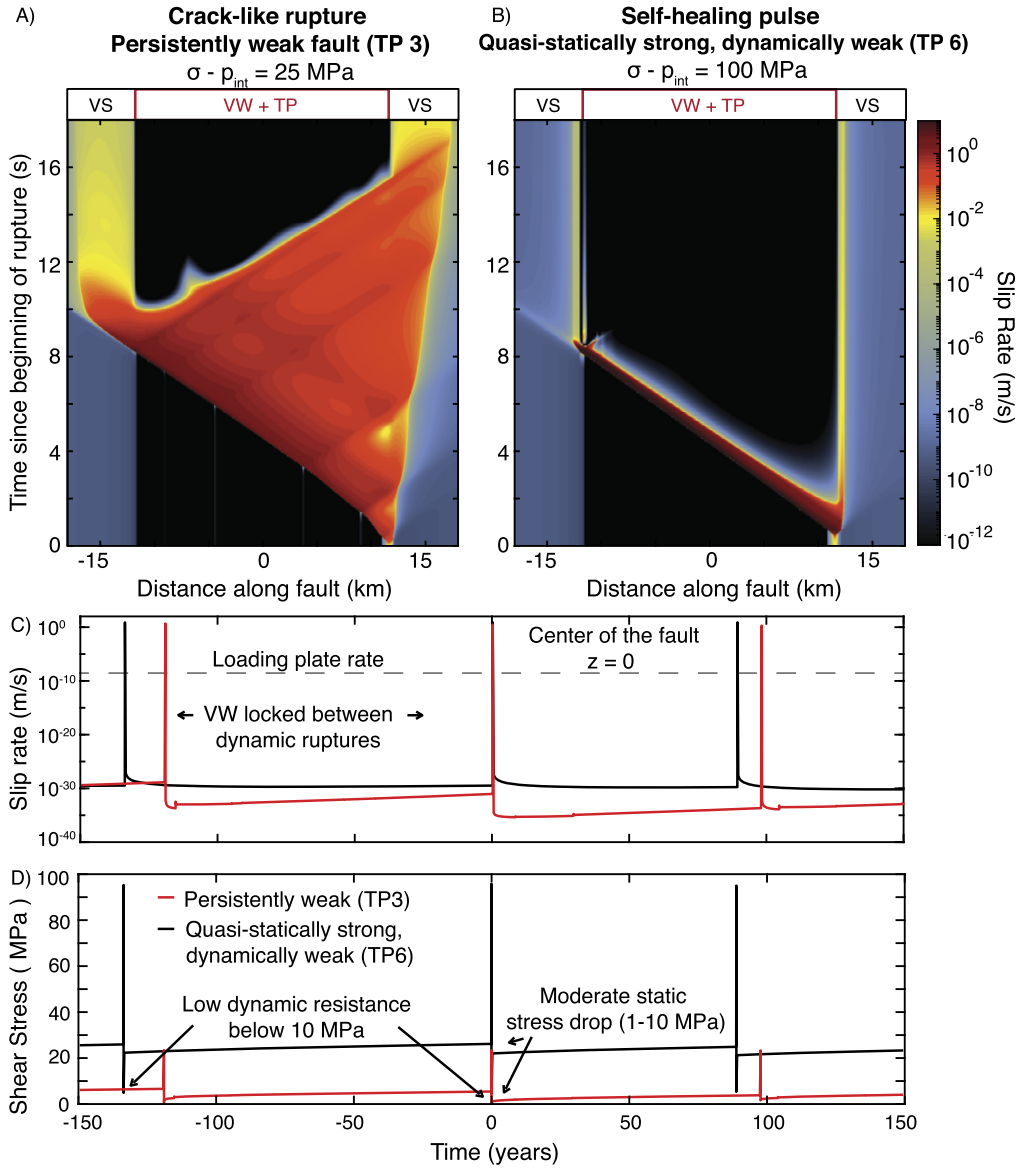

Fig. 1. Evolution of slip rate and shear stress with time for representative fault models hosting crack-like (fault model TP3 from Supplementary Table 2) and self-healing pulse-like (fault model TP6) ruptures. (A-B) The fault models are composed of a velocity-weakening (VW) seismogenic region surrounded by two velocity-strengthening (VS) sections. Local seismic slip duration during (A) crack-like ruptures is proportional to the overall rupture duration whereas only a small portion of the fault slips at a given time during (B) self-healing pulse-like ruptures. (C-D) Evolution of local slip rate and shear stress at the center of the fault over sequences of earthquakes with low dynamic resistance and moderate static stress drops. Time series are centered at t=0 corresponding to the ruptures shown in (A-B). (C) Most points within the VW region are locked during the interseismic period between dynamic ruptures, with slip rates far below the loading plate rate. (D) The shear stress over the persistently weak fault model (TP3) which hosts the crack-like rupture is always low ($<$ 20 MPa). For self-healing pulse-like ruptures on quasi-statically strong, dynamically weak fault model (TP6), the shear stress before the rupture is relatively high compared to the persistently weak fault ($>$ 30 MPa), then drops to low values below 10 MPa during seismic slip, and recovers to around 20 MPa over most of the ruptured region.

be inferred from shear-heating constraints), and seismologically inferable source properties, such as the static stress drop and apparent stress. We then analyze our simulations with a focus on the average stress values (section 4) and show that the energy-based shear stress is significantly higher for self-healing pulses, due to their higher apparent stress, in comparison with crack-like ruptures of the same average stress drop and slip. While averaged shear stresses for crack ruptures are within one static stress drop from the dissipation-based average shear stress, the averaged shear stresses before and after self-healing pulses can be 2-4 static stress drops higher than shear stresses related to shear heating, providing a potential physical explanation for higher estimates of fault stress based on geodynamics and topography. We discuss related seismological observations in section 5 and conclusions in section 6.

2. Numerical simulations of crack-like versus self-healing pulse-like ruptures

2.1. Model description

We conduct numerical simulations of sequences of earthquakes and aseismic slip following the methodological developments of Lapusta et al. (2000), Noda and Lapusta (2010), and Lambert et al. (2021b). Our simulations consider mode III slip on a 1-D fault embedded into a 2-D uniform, isotropic, elastic medium (Supplementary Figure S1). The resulting slip on the fault includes sequences of earthquakes and aseismic slip, including the nucleation process, dynamic rupture propagation, postseismic slip that follows each seismic event, and interseismic period between seismic events that

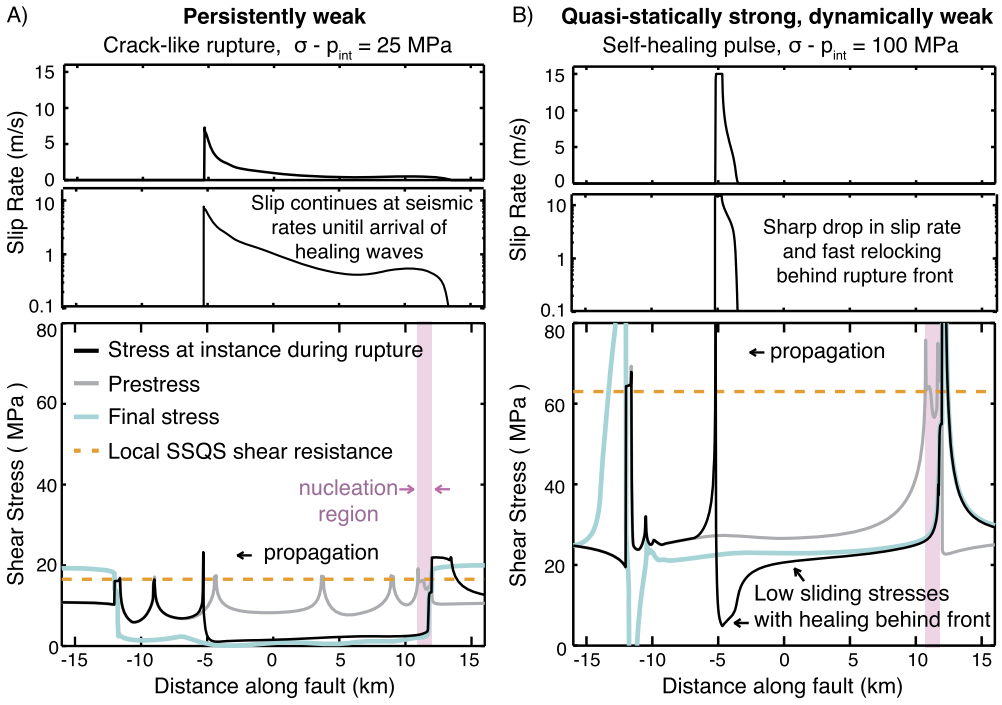

Fig. 2. Spatial distribution of slip rate (top) and shear stress (bottom) for the same representative ruptures as in Fig. 3. Both ruptures nucleate with prestress levels (gray line) that are near the local steady-state quasi-static shear resistance (dashed orange line), however the ruptures propagate over lower prestress conditions depending on the efficiency of weakening. The slip rate and shear stress at the same instance are shown by the black lines, illustrating the concentrated stress changes at the rupture front, with slip continuing throughout the entirety of the rupture for the crack-like rupture (A), but not the self-healing pulse (B).

can last up to tens or hundreds of years and host steady and transient slow slip.

Our fault models are governed by a form of the laboratory-derived Dieterich-Ruina rate-and-state friction law (Dieterich, 1979; Ruina, 1983) as well as enhanced dynamic weakening during rapid slip due to the thermal pressurization of pore fluids (Sibson, 1973; Rice, 2006, further details in the Supplementary Text). The effects of off-fault yielding are approximated through a limit on slip velocity (Supplementary Text). The simulated fault contains a 24-km region Ω_{vw} with velocity-weakening (VW) frictional properties where earthquakes can nucleate and propagate, surrounded by velocity-strengthening (VS) regions that inhibit rupture propagation (Fig. 1). The fault is loaded by a region outside these frictional regions slipping at a prescribed tectonic plate rate. We refer to ruptures that span the entire VW region and arrest in the VS region as model-spanning ruptures. We define the beginning and end of dynamic rupture, t_{ini} and t_{fin} respectively, as well as the ruptured region Ω_{rupt}, using a slip-velocity threshold ($V_{\text{thresh}} = 1$ cm/s) for seismic slip, based on previous studies (Perry et al., 2020; Lambert et al., 2021b).

We study the evolution of shear stress and average stress measures in fault models which produce ruptures with typically observed static stress drops of 1-10 MPa (e.g. Shearer et al., 2006; Allmann and Shearer, 2009; Ye et al., 2016) and which are consistent with low heat production, where the shear stresses associated with shear heating are below 20 MPa. We conduct simulations with varying levels of background fluid overpressure in terms of the effective normal stress, as well as varying degrees of efficiency in enhanced weakening due to thermal pressurization. The parameter values we have chosen (Supplementary Tables S1 - S2) are motivated by prior studies (Rice, 2006; Noda and Lapusta, 2010; Perry et al., 2020; Lambert et al., 2021b) and our goal of examining ruptures with varying efficiency in enhanced dynamic weakening and different rupture styles.

For realistic, lab-derived fault constitutive relations such as rate-and-state friction, the concept of a local "static friction" coefficient that must be reached for the slip to occur is ill-defined, since slip rate is non-zero for any non-zero shear stress. We choose a representative value for the classical notion of local quasi-static fault strength, which we call the local steady-state quasi-static (SSQS) shear resistance and define as the product of the interseismic drained effective normal stress and the quasi-static friction coefficient during steady creep $f_{ss}(V)$ at the prescribed tectonic plate rate V_{pl}:

$$\tau_{ss}^{V_{\text{pl}}}(z,t) = (\sigma - p_{\text{int}})\, f_{ss}(V_{\text{pl}}). \tag{1}$$

Here σ is the normal stress and "drained" refers to the effective stress with ambient interseismic pore pressure p_{int} unaffected by slip processes such as dilatancy or thermal pressurization. Previous numerical studies have shown that the local SSQS shear resistance $\tau_{ss}^{V_{\text{pl}}}$ is comparable to the spatially-averaged prestress during rupture nucleation (Supplementary Figure S2; Lambert et al., 2021a).

2.2. Local fault behavior in simulated crack-like and self-healing pulse-like ruptures

All of our simulated ruptures nucleate in regions with locally high prestress near the corresponding local SSQS resistance, but then propagate over areas of varying, and particularly lower, prestress conditions depending on the efficiency of dynamic weakening (Fig. 2; Lambert et al., 2021a,b). For persistently weak faults, the shear stress is always low (< 20 MPa; Fig. 1D). In contrast, the local shear resistance on quasi-statically strong, dynamically weak faults, and hence the local shear stress, is generally higher during periods of negligible motion before and after ruptures, and quite high at the peak of the propagating rupture, but drops dramatically to lower values below 10 MPa during most of seismic slip (Figs. 1C-D); in these models, ruptures with realistic stress drops tend to be pulse-like (Lambert et al., 2021b)

In crack-like ruptures, the local shear resistance drops at high slip rates and remains low throughout the remainder of the rup-

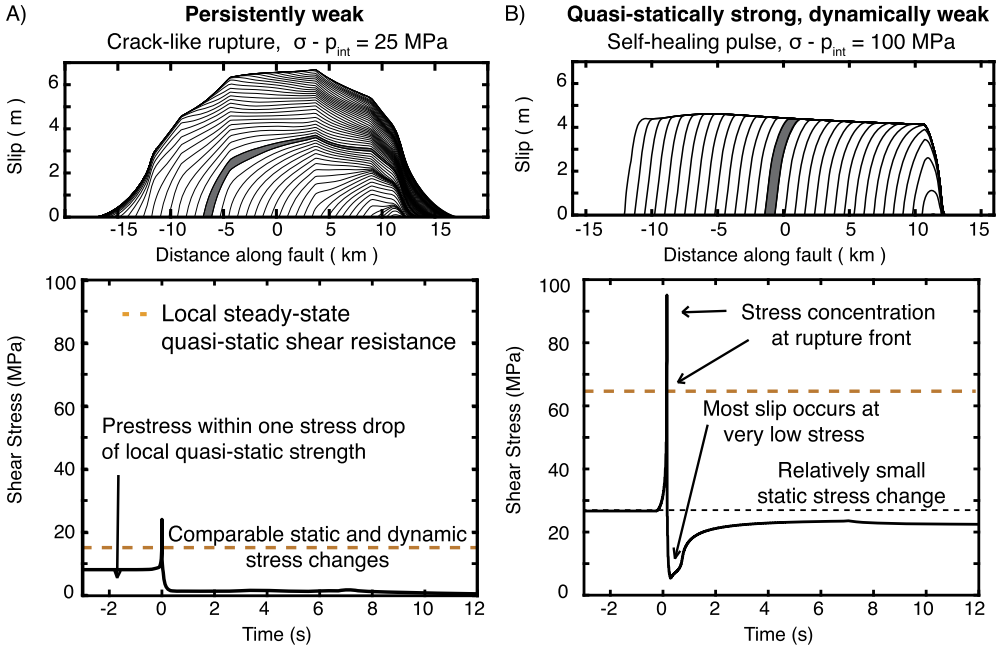

Fig. 3. Evolution of slip and local shear stress with time throughout characteristic a crack-like rupture and self-healing pulse. (Top) Characteristic evolution of slip along the fault for (A) a crack-like rupture and (B) a self-healing pulse in persistently weak (TP 3) and quasi-statically strong, dynamically weak (TP 6) fault models, respectively. Slip contours are plotted every 0.25 s and the gray shading illustrates a portion of the fault that is slipping during a 0.25-second interval. (Bottom) The local evolution of shear stress with time at a point in the center of the fault (z = 0 km), in the representative ruptures. The stress concentration at the rupture front is much larger for the ruptures with more efficient weakening on quasi-statically strong, dynamically weak behavior (B) than for the ruptures with more moderate weakening on persistently weak faults (A). The self-healing pulses (B) experience rapid healing resulting in dynamic stress variations that are much larger than the static stress change.

ture process (Fig. 3A). Points along the fault continue to slip until the arrival of arrest waves with opposite stress polarity from the edges of the rupture (Fig. 2A). The final shear stress post-slip is typically adjusted by the waves to be slightly lower than the typical shear stress during sliding (Figs. 2A; Madariaga, 1976; Lambert et al., 2021b), a situation called "overshoot." The overshoot is typically minor, i.e., a small fraction of the final static stress change (Madariaga, 1976; Beeler et al., 2003; Kanamori and Rivera, 2006; Lambert et al., 2021b), and is typically ignored, although some recent studies have noted the potentially non-negligible contribution of the overshoot to the energy balance (Ke et al., 2022).

In contrast, the arrest of slip during a self-healing pulse occurs due to local healing or restrengthening of the shear resistance independent of the arrival of arrest waves (e.g. Heaton, 1990; Noda et al., 2009; Lambert et al., 2021b), such as from the drop in shear heating due to decreasing local slip rates and diffusion of pore fluids in the case of enhanced weakening due to thermal pressurization, as in our models. In this case, the increase in dynamic stress due to fault slip elsewhere is balanced by local healing, allowing the local slip to arrest while the rupture proceeds elsewhere. Due to the presence of rapid healing, self-healing pulses exhibit a dynamic stress undershoot, with the final shear stress being higher than the local shear resistance during sliding (Figs. 2B and 3B; Beeler et al., 2003; Heaton, 1990; Lambert et al., 2021b). This also means that the dynamic stress drop is significantly larger than the static stress drop. The undershoot can be quite significant, comparable to the static stress drop or even several times larger, increasing for sharper self-healing pulses (Lambert et al., 2021b). In this study, we explore how the presence of this undershoot modifies the average stress on faults.

3. Average shear stress measures related to earthquake energy partitioning

To relate these complex local fault behaviors to thermal or seismological observables that typically encapsulate the entire rupture, one needs to consider appropriate averaging. There are different methods for averaging the shear stress along a fault over space and time, as discussed in Noda and Lapusta (2012) and the Supplementary Text. In part, one can consider the spatially-averaged shear stress, which is a straightforward spatial average of shear stress along a fault, denoted here as τ^A. In this work, we focus on energy-based average shear stress, $\overline{\tau}^E$, for earthquake ruptures, which is a weighted average based on energy considerations (Summary of key quantities shown in Supplementary Table S3). We find that the energy-based stress averages are comparable to spatially-averaged ones for our models (Supplementary Figures S2-4). We propose that energy-based stress measures are more useful to consider as they (1) can in principle be inferred from seismological observations and thermal considerations, as we discuss in the following, and (2) are more physically relevant to notions of fault strength: the energy-based averages are, by definition, the physically relevant average shear stress measures for the work done to impose slip along a fault, and therefore may best represent the overall average shear resistance along the fault to external loading.

The energy-based definition of average fault stresses follows from the energy balance (Beeler et al., 2003; Noda and Lapusta, 2012; Noda et al., 2013). For a given earthquake rupture, the associated strain energy change ΔW is partitioned into the energy E_{Diss} dissipated within the ruptured source region and the energy E_R radiated away to the far-field:

$$\Delta W/A = E_{\text{Diss}}/A + E_R/A, \tag{2}$$

where the relation is expressed per unit rupture area A. The strain energy change represents the work done to transition from an initial to final stress state over an average slip $\overline{\delta}_{\text{rupt}}$ and it can be expressed as (Supplementary Text; Noda and Lapusta, 2012):

$$\Delta W/A = \frac{1}{2}\left[\overline{\tau}^E_{\text{ini}} + \overline{\tau}^E_{\text{fin}}\right]\overline{\delta}_{\text{rupt}}, \tag{3}$$

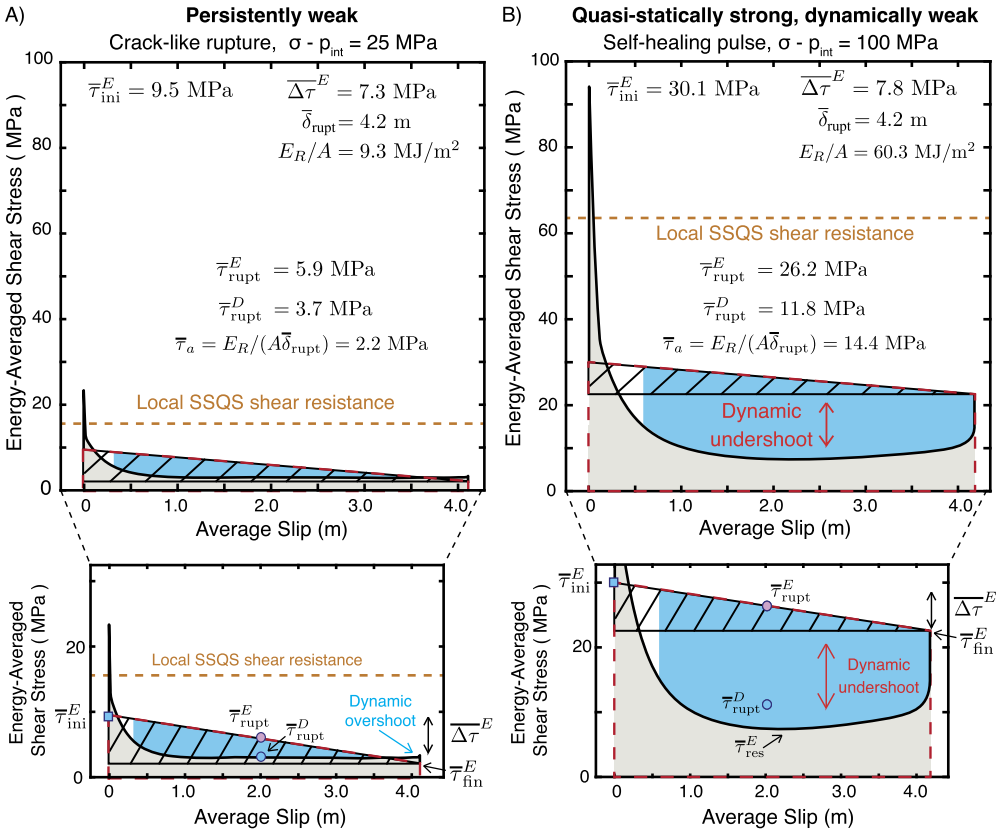

Fig. 4. The energy-averaged shear stress vs. slip for the same representative ruptures as in Fig. 3, illustrating the energy budget of each rupture. The crack-like rupture on the persistently weak fault (A) and the self-healing pulse on the quasi-statically strong, dynamically weak fault (B) have comparable static stress drop and average slip, and hence seismologically-inferable available energy $\overline{\Delta\tau}^E\overline{\delta}_{\rm rupt}/2$ (slashed black triangle). The total strain energy change (dashed red trapezoid) is partitioned into radiated energy (blue shading), and dissipated energy (gray shading). (A) For crack-like ruptures, the average static and dynamic stress drops are comparable, with a relatively small dynamic overshoot. (B) The self-healing pulse experiences rapid healing resulting in average dynamic stress variations that are much larger than the average static stress change, and hence radiate more energy for the same average slip and static stress drop as the crack-like rupture. For both ruptures, the additional dissipation associated with the initial strengthening outside of the red trapezoid comes at the expense of the radiated energy (white triangle inside the dashed red trapezoid).

where $\overline{\tau}^E_{\rm ini}$ and $\overline{\tau}^E_{\rm fin}$ denote averages of shear stresses at the beginning and end of rupture, weighted by the final slip; they are given by:

$$\overline{\tau}^E_{\rm ini} = \frac{\int_{\Omega_{\rm rupt}} \tau_{\rm ini}(z)\delta_{\rm rupt}(z)dz}{\int_{\Omega_{\rm rupt}} \delta_{\rm rupt}(z)dz}, \overline{\tau}^E_{\rm fin} = \frac{\int_{\Omega_{\rm rupt}} \tau_{\rm fin}(z)\delta_{\rm rupt}(z)dz}{\int_{\Omega_{\rm rupt}} \delta_{\rm rupt}(z)dz}. \quad (4)$$

Here and in the following, we provide expressions for a 1D fault; full expressions for a 2D fault are given in Noda and Lapusta (2012). We refer to these averages of the initial and final shear stresses as the energy-based averages; from them, one can define an energy-based stress drop $\overline{\Delta\tau}^E$ (Noda et al., 2013) and energy-based average rupture stress $\overline{\tau}^E_{\rm rupt}$ as:

$$\overline{\Delta\tau}^E = \overline{\tau}^E_{\rm ini} - \overline{\tau}^E_{\rm fin} \quad (5)$$

$$= \frac{\int_{\Omega_{\rm rupt}} \Delta\tau(z)\delta_{\rm rupt}(z)dz}{\int_{\Omega_{\rm rupt}} \delta_{\rm rupt}(z)dz}. \quad (6)$$

$$\overline{\tau}^E_{\rm rupt} = \frac{1}{2}\left[\overline{\tau}^E_{\rm ini} + \overline{\tau}^E_{\rm fin}\right] \quad (7)$$

$$= \frac{1}{2}\frac{\int_{\Omega_{\rm rupt}} [\tau_{\rm ini}(z) + \tau_{\rm fin}(z)]\delta_{\rm rupt}(z)dz}{\int_{\Omega_{\rm rupt}} \delta_{\rm rupt}(z)dz} \quad (8)$$

An energy-based weighting procedure can be used to construct an averaged shear stress versus slip diagram (Fig. 4) which both represents the energy partitioning during rupture as well as aims to preserve the features of the local evolution of shear stress vs. slip, such as undershoot (Noda and Lapusta, 2012). In the diagram, the area under the curve is equal to the dissipated energy per unit fault area; the initial and final stresses are given by their energy-based averages, $\overline{\tau}^E_{\rm ini}$ and $\overline{\tau}^E_{\rm fin}$ respectively; and they allow to construct the trapezoid illustrating the strain energy released per unit area.

From equations (2)-(8), the energy-based average rupture stress $\overline{\tau}^E_{\rm rupt}$ can be expressed as the sum of the dissipation-based average rupture stress $\overline{\tau}^D_{\rm rupt} = E_{\rm Diss}/(\overline{\delta}_{\rm rupt}A)$ and the apparent stress $\overline{\tau}_a = E_R/(\overline{\delta}_{\rm rupt}A)$ (Wyss and Brune, 1968; Lachenbruch and Sass, 1980; Beeler et al., 2003, further details in Supplementary Text):

$$\overline{\tau}^E_{\rm rupt} = \frac{E_{\rm Diss}}{A\overline{\delta}_{\rm rupt}} + \frac{E_R}{A\overline{\delta}_{\rm rupt}} \quad (9)$$

$$= \overline{\tau}^D_{\rm rupt} + \overline{\tau}_a \quad (10)$$

Assuming that most of the dissipated energy during rupture occurs around the fault, $\overline{\tau}^D_{\rm rupt}$ represents the average dynamic shear resistance localized along the interface. $\overline{\tau}^E_{\rm rupt}$ includes both this average dynamic resistance $\overline{\tau}^D_{\rm rupt}$ as well as the contribution from inertial resistance during dynamic rupture. This additional resistance, which is represented by the apparent stress $\overline{\tau}_a$, is sometimes referred to as the radiation resistance (Savage and Wood, 1971):

$$\overline{\tau}_a = \frac{E_R}{A\overline{\delta}_{\rm rupt}} = \frac{\mu E_R}{M_o}, \quad (11)$$

where M_o is the seismic moment. For quasi-static processes where the radiated energy is negligible, the energy-based rupture stress $\overline{\tau}^E_{\text{rupt}}$ is equivalent to the dissipation-based dynamic resistance $\overline{\tau}^D_{\text{rupt}}$.

The dissipation-based dynamic resistance $\overline{\tau}^D_{\text{rupt}}$ represents all contributions to the dissipated energy throughout the rupture process, including dissipated energy that is converted into heat as well as energy consumed in the generation of new fracture surfaces or chemical processes. One can further partition $\overline{\tau}^D_{\text{rupt}}$ in equation (10) to consider contributions to the energy-based rupture stress from dissipation associated with heat production, $\overline{\tau}^{\text{D,heat}}_{\text{rupt}}$, and all other dissipative processes $\overline{\tau}^{\text{D,other}}_{\text{rupt}}$:

$$\overline{\tau}^E_{\text{rupt}} = \overline{\tau}^{\text{D,heat}}_{\text{rupt}} + \overline{\tau}^{\text{D,other}}_{\text{rupt}} + \overline{\tau}_a \tag{12}$$

It is commonly assumed that the majority of the dissipated energy during earthquake ruptures is converted into heat, with the contribution from other sources of the dissipation being relatively small, i.e. $\overline{\tau}^{\text{D,other}}_{\text{rupt}} \ll \overline{\tau}^{\text{D,heat}}_{\text{rupt}}$. This assumption is supported by some laboratory and field measurements which suggest that the portion of dissipated energy not converted into heat may indeed be small, $< 3\%$ (Chester et al., 2005; Aben et al., 2019). We proceed in the following with this assumption and revisit it in the discussion.

Assuming that most of the dissipation during earthquake ruptures is converted into heat, the dissipation-based dynamic resistance $\overline{\tau}^D_{\text{rupt}}$ can, in principle, be inferred from heat-flow measurements. While this may be difficult to accomplish for a single rupture, the long-term constraints on shear-heating stress based on heat flow near mature faults, such as less than 10-20 MPa discussed in the introduction, may be a relevant stand-in for large dynamic ruptures. In our simulations, we define the shear heating stress $\overline{\tau}^D_{\text{heat}}$ to be equal to the cumulative dissipation-based average shear stress over the VW seismogenic region, which is consistent with the shear stress averaged over seismogenic depths inferred from heat flow measurements around faults (Noda and Lapusta, 2012):

$$\overline{\tau}^D_{\text{heat}}(t) = \frac{\int_0^t \int_{\Omega_{\text{vw}}} \tau(z,t') V(z,t') dz dt'}{\int_0^t \int_{\Omega_{\text{vw}}} V(z,t') dz dt'}. \tag{13}$$

Our simulations show that $\overline{\tau}^D_{\text{heat}}$ is a good approximation of $\overline{\tau}^D_{\text{rupt}}$ for large earthquake ruptures (section 4).

The energy-based average shear stress $\overline{\tau}^E_{\text{rupt}}$ can then, in principle, be inferred from thermal constraints through $\overline{\tau}^D_{\text{rupt}} \approx \overline{\tau}^D_{\text{heat}}$ and remote inferences of earthquake rupture properties - radiated energy, seismic moment, and shear modulus - that contribute to apparent stress (equation (11)). The energy-based prestress before a rupture, $\overline{\tau}^E_{\text{ini}}$, can then be determined from $\overline{\tau}^E_{\text{rupt}}$ plus half the energy-based static stress drop $\overline{\Delta\tau}^E$:

$$\overline{\tau}^E_{\text{ini}} = \overline{\tau}^E_{\text{rupt}} + \overline{\Delta\tau}^E/2 \tag{14}$$

$$= \overline{\tau}^D_{\text{rupt}} + \overline{\tau}_a + \overline{\Delta\tau}^E/2 \tag{15}$$

$$= \overline{\tau}^{\text{D,heat}}_{\text{rupt}} + \overline{\tau}^{\text{D,other}}_{\text{rupt}} + \overline{\tau}_a + \overline{\Delta\tau}^E/2. \tag{16}$$

Equation (16) indicates the potential sources of discrepancy between the geodynamic and similar estimates of average fault prestress, which reflect $\overline{\tau}^E_{\text{ini}}$, and fault stresses based on shear heating constraints, represented here by $\overline{\tau}^{\text{D,heat}}_{\text{rupt}}$. The two differ by the apparent stress $\overline{\tau}_a$; stresses $\overline{\tau}^{\text{D,other}}_{\text{rupt}}$ that represent the non-heat dissipation; and half the static stress drop. In the following section, we show that self-healing pulses can theoretically account for the discrepancy by their potential to have large $\overline{\tau}_a$.

Note that the relevant definition of static stress drop for comparison with energy considerations is the energy-based - or slip-weighted - static stress drop (equation (6)). The slip-weighted stress drop has been shown to be greater than or equal to standard moment-based estimates of static stress drop from seismological inferences; the two stress drops are similar for relatively uniform fault slip and diverge for increasingly non-uniform slip (Noda et al., 2013).

4. Average stresses for simulated cracks and self-healing pulses

4.1. Relationship between average stress measures and shear heating for cracks and self-healing pulses

Our simulations highlight that the relationship between the dissipation-based rupture stress $\overline{\tau}^D_{\text{rupt}}$ and other average stress measures substantially depends on the style of rupture propagation.

For crack-like ruptures, the dissipation-based rupture stress $\overline{\tau}^D_{\text{rupt}}$ is within one static stress drop of the averaged stresses before ($\overline{\tau}^E_{\text{ini}}$) and during ($\overline{\tau}^E_{\text{rupt}}$) the rupture (Figs. 4A-6A). This is because the final and dynamic stress levels are comparable for crack-like ruptures, and a considerable portion of the total rupture area is slipping and dissipating energy at a given time (Figs. 1A & 2A top). In addition, $\overline{\tau}^D_{\text{rupt}}$ is higher than the energy-based final stress $\overline{\tau}^E_{\text{fin}}$ for crack-like ruptures (yellow vs. light red in Fig. 5A), creating dynamic overshoot (Fig. 4A).

As the cumulative dissipation, and hence associated shear heating stress $\overline{\tau}^D_{\text{heat}}$, across the VW region in our models is dominated by the dissipation during large model-spanning earthquakes, the shear-heating stress $\overline{\tau}^D_{\text{heat}}$ is nearly equal to the dissipation-based average rupture stress $\overline{\tau}^D_{\text{rupt}}$ (Fig. 6A). Fault models with relatively mild weakening produce predominantly crack-like ruptures and maintain average stress levels closer to the local SSQS shear resistance $\tau_{ss}^{V_{\text{pl}}}$ (Figs. 2A and 6A). To maintain low values of the dissipation-based average rupture stress $\overline{\tau}^D_{\text{rupt}}$, and thus low shear heating stresses (Fig. 6A), models with crack-like ruptures require chronically weak fault conditions, such as through increased pore fluid pressure as in this study or low quasi-static friction.

In contrast, for self-healing pulses, the dissipation-based rupture stress $\overline{\tau}^D_{\text{rupt}}$ can be several static stress drops below the averaged stresses before ($\overline{\tau}^E_{\text{ini}}$) and during ($\overline{\tau}^E_{\text{rupt}}$) the rupture (Figs. 4B, 5B-C and 6B). Moreover, $\overline{\tau}^D_{\text{rupt}}$ can be much lower than the average final stress $\overline{\tau}^E_{\text{fin}}$ (yellow vs. red in Fig. 5B-C). This is because only a small portion of the fault slips at a given time and the level of dynamic resistance is much lower than the final stress after healing (Figs. 1B and 2B). As such, the fault can sustain substantially higher averaged prestresses and final stresses, while still maintaining low levels of dynamic resistance and producing realistic average static stress drops (Figs. 4B & 6B).

Overall, we find that the dissipation-based stress averages $\overline{\tau}^D_{\text{rupt}}$ and $\overline{\tau}^D_{\text{heat}}$, which are similar in our models, provide lower bounds for the spatially-averaged and energy-averaged shear stress on the fault. How much larger can the spatially- and energy-averaged shear stress be depends on the degree of stress undershoot. The sharper the self-healing pulse, the larger the undershoot and apparent stress, and hence the larger the average rupture prestress compared to the average dissipation-based shear stress (Figs. 6 and 7).

The apparent stress $\overline{\tau}_a$ has commonly been associated with the static stress drop in seismological analyses (McGarr, 1999; Perez-Campos and Beroza, 2001; Ide and Beroza, 2001) and is sometimes used as a constraint for inversions of static stress drop, where it is assumed that the static stress drop must be larger than the

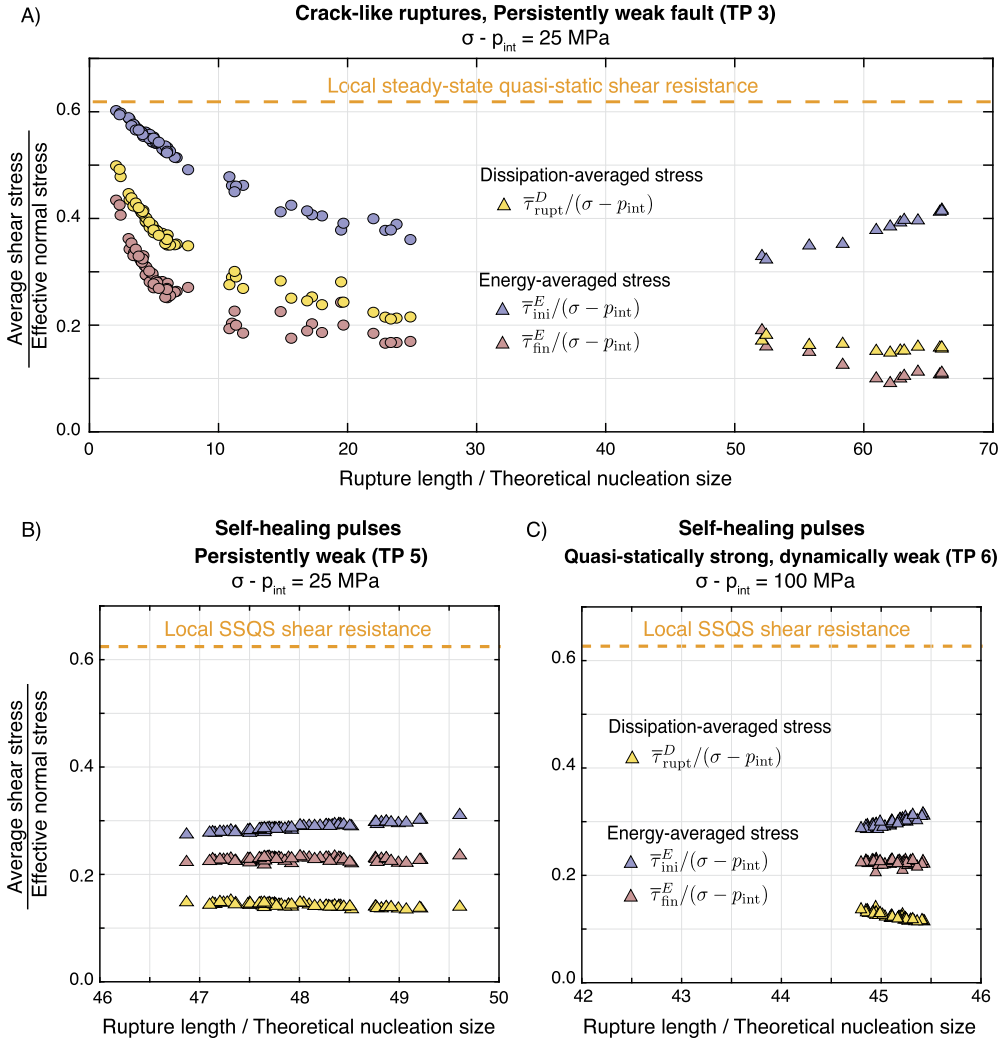

Fig. 5. Comparison of the dissipation-based dynamic resistance and energy-based average pre-rupture and final shear stresses for crack-like and self-healing pulse-like ruptures. (A) For crack-like ruptures, the dissipation-based average rupture stress $\overline{\tau}^D_{\rm rupt}$ (yellow) - a measure of the average dynamic shear resistance - is higher than the energy-based final stress $\overline{\tau}^E_{\rm fin}$ (pink) due to the presence of a dynamic stress overshoot after rupture arrest. (B-C) In contrast, for self-healing pulses, the dissipation-based average rupture stress is lower than the energy-based final stress due to the presence of a dynamic undershoot. Thus, the energy-based static stress drop ($\overline{\Delta\tau}^E = \overline{\tau}^E_{\rm ini} - \overline{\tau}^E_{\rm fin}$) can substantially underestimate the difference between the energy-based pre-rupture stress and dissipation-based average dynamic resistance for self-healing pulse-like ruptures, whereas the average static stress drop is more comparable or may even overestimate the average dynamic stress drop for crack-like ruptures.

apparent stress, consistent with a dynamic stress overshoot for crack-like ruptures (Savage and Wood, 1971; Wei and McGuire, 2014). Our simulations illustrate that this need not be the case as dynamic stress changes can be considerably larger than the static stress changes for self-healing pulses. The ratio of the apparent stress to average static stress drop is proportional to the seismically-inferable radiation ratio $\eta^{\rm inf}_R$, sometimes referred to as the radiation efficiency or Savage-Wood efficiency, which is defined as the ratio of the radiated energy to the product of half the average static stress drop, slip and rupture area (Savage and Wood, 1971; Kanamori and Brodsky, 2004; Lambert et al., 2021b):

$$\eta^{\rm inf}_R = \frac{E_R/A}{\frac{1}{2}\overline{\Delta\tau}^E \overline{\delta}_{\rm rupt}} = \frac{2\overline{\tau}_a}{\overline{\Delta\tau}^E}. \tag{17}$$

Another way to think about $\eta^{\rm inf}_R$ is as a non-dimensional (or scaled) radiated energy. Note that, for crack-like ruptures, the product of the average static stress drop and slip is a close approximation to the energy per unit area available for breakdown energy at the rupture tip and radiated energy, and hence the product is sometimes called "available energy" (Kanamori and Brodsky, 2004; Lambert et al., 2021b); in that case, $\eta^{\rm inf}_R$ represents the relative proportion of radiated energy in the available energy and can be called "radiation efficiency." However, for self-healing slip pulses, much more additional energy can be available for radiation, and the values of $\eta^{\rm inf}_R$ can be substantially higher than 1 (Fig. 8a, Lambert et al., 2021b).

The difference between the energy-averaged prestress $\overline{\tau}^E_{\rm ini}$ and the dissipation-based average rupture stresses $\overline{\tau}^D_{\rm rupt}$ can then be expressed, from equation (15), in terms of the apparent stress and energy-based static stress drop or, equivalently, in terms of the seismically-inferable radiation ratio and energy-based static stress drop:

$$\overline{\tau}^E_{\rm ini} - \overline{\tau}^D_{\rm rupt} = \overline{\tau}_a + \overline{\Delta\tau}^E/2 \tag{18}$$

$$= \frac{\left(\eta^{\rm inf}_R + 1\right)}{2}\overline{\Delta\tau}^E. \tag{19}$$

Sharper self-healing pulses result in higher apparent stresses $\overline{\tau}_a$ and radiation ratios $\eta^{\rm inf}_R$, and can thus have notably greater differences between the energy-based average prestress and dissipation-

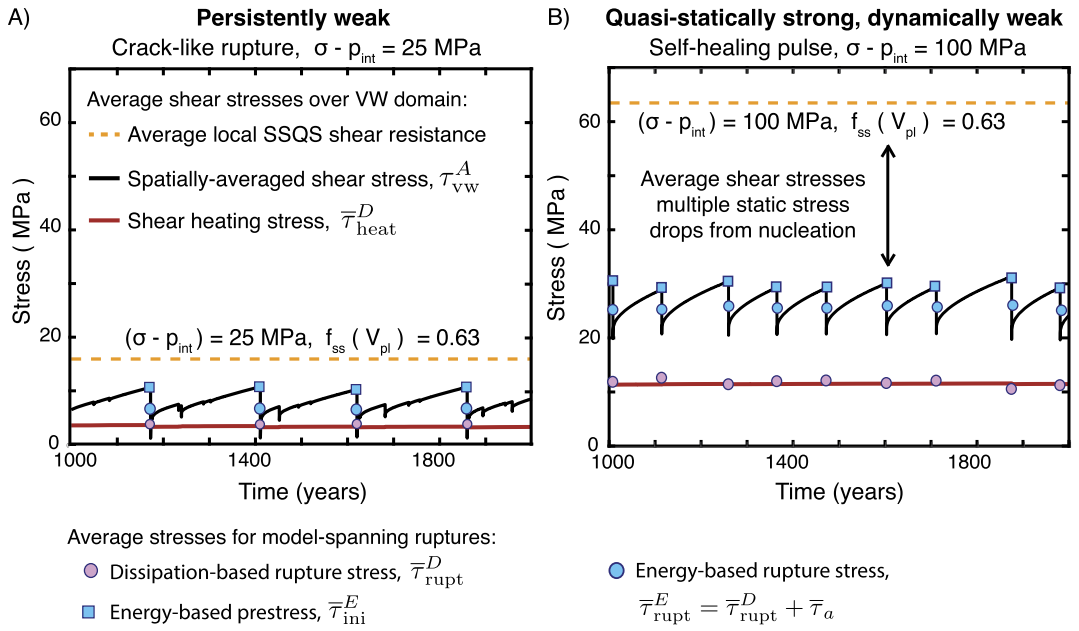

Fig. 6. The evolution of average shear stress in the VW region over sequences of events for the two fault models shown in Fig. 3. The spatially-averaged shear stress $\tau^A_{\rm vw}$ over the VW region for the chronically weak fault producing crack-like ruptures (A) is always within 1-2 static stress drops from the average local SSQS shear resistance (orange line), whereas the average shear stress is far below the average local SSQS shear resistance for models exhibiting dynamically weak behavior (B). The dissipation-based stress $\overline{\tau}^D_{\rm rupt}$ from large VW-segment spanning earthquakes (pink circles) is consistent with the shear heating stress, which provides a lower bound of the average shear stress $\tau^A_{\rm vw}$. The energy-based prestress $\overline{\tau}^E_{\rm ini}$ and rupture stress $\overline{\tau}^E_{\rm rupt}$ from large VW-segment spanning earthquakes (blue squares and circles, respectively) provide a reasonable description of the spatially-averaged shear stress before large ruptures and throughout earthquake sequences, independent of the style of rupture.

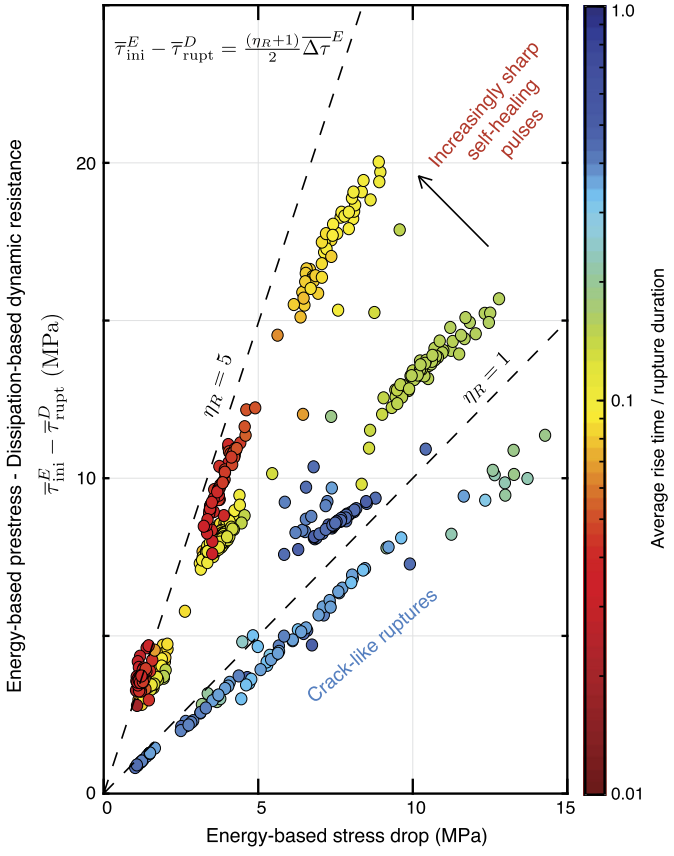

Fig. 7. Difference between the energy-averaged prestress $\overline{\tau}^E_{\rm ini}$ and dissipation-based average dynamic resistance $\overline{\tau}^D_{\rm rupt}$ versus static stress drop for self-healing pulses and crack-like ruptures. The difference between $\overline{\tau}^E_{\rm ini}$ and $\overline{\tau}^D_{\rm rupt}$ is proportional to the static stress drop through the radiation ration η_R, which is much larger for sharper self-healing pulses with shorter rise time to rupture durations (warmer colors).

based rupture stress compared to crack-like ruptures with similar static stress drops (Fig. 7).

We note that the dissipation-based rupture stress $\overline{\tau^D}_{\rm rupt}$, which represents the average dynamic shear resistance to motion on the fault during rupture, decreases with increasing rupture size and average slip in our models in a manner consistent with observations of enhanced dynamic weakening in the lab (Fig. 5 and Supplementary Figure S3; e.g. Di Toro et al., 2011). This decrease in averaged stress with increasing rupture size and efficiency of weakening behavior is similarly observed for the spatial and energy-based prestress (Fig. 5 and Supplementary Figures S2-3; Lambert et al., 2021a).

4.2. Estimates of energy-averaged prestress with input from numerical and lab modeling

Let us build on the energy considerations of section 3 to develop another representation for the energy-averaged prestress $\overline{\tau}^E_{\rm ini}$ that can help estimate the prestress with inputs from numerical and lab modeling. The total dissipated energy per unit rupture area can be partitioned into the average breakdown energy G and residual dissipated energy $E_{\rm F}/A$ below the minimum average shear stress during sliding (Palmer and Rice, 1973; Kanamori and Brodsky, 2004; Ye et al., 2016). This residual dissipated energy is represented by the area under the minimum stress level $\overline{\tau}^E_{\rm res}$ of the energy-averaged stress versus slip diagram, i.e. $E_F/A = \overline{\tau}^E_{\rm res}\overline{\delta}_{\rm rupt}$ (Fig. 4). The sum of the strain energy change available for the breakdown process and radiation is referred to as the available energy $\Delta W_0/A = G + E_R/A$, which is thought to represent the energy relevant to the dynamics of the rupture (Kanamori and Brodsky, 2004). The energy-averaged prestress $\overline{\tau}^E_{\rm ini}$ can be determined from the available energy ΔW_0, potency $\overline{\delta}_{\rm rupt}A$, energy-based static stress drop $\overline{\Delta\tau}^E$, and insight into the residual stress level $\overline{\tau}^E_{\rm res}$:

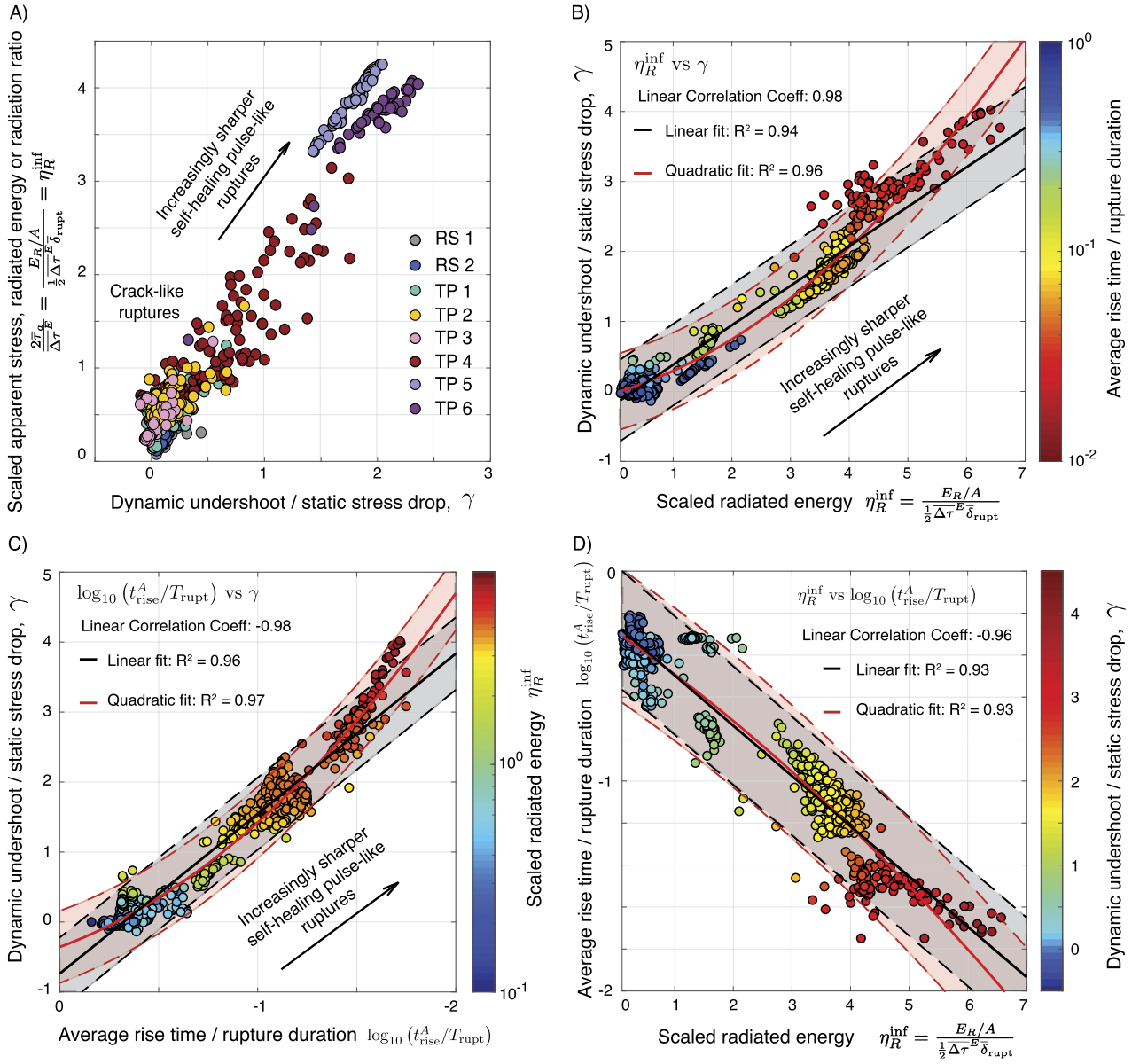

Fig. 8. Relation between scaled undershoot γ, scaled radiated seismic energy (or apparent stress $2E_R/(\overline{\Delta\tau}^E\overline{\delta}_{\text{rupt}}A) = 2\overline{\tau}_a/\overline{\Delta\tau}^E$ equal to seismologically-inferable radiation ratio η_R^{inf}) and the logarithm of average rise time to rupture duration $\log_{10}(t^A_{\text{rise}}/T_{\text{rupt}})$ based on modeling results of Lambert et al. (2021b). (A) The ratio of apparent stress to energy-based static stress drop increases for ruptures that experience larger average dynamic undershoot with respect to the static stress drop. Crack-like ruptures typically result in mild stress overshoot/undershoot whereas sharp self-healing pulses experience a substantial stress undershoot and radiation ratios greater than 1. (B-D) Linear and quadratic fits to trends. (B) Scaled radiated energy η_R^{inf} vs scaled dynamic undershoot γ. (C) Average rise time to rupture duration $t^A_{\text{rise}}/T_{\text{rupt}}$ vs scaled dynamic undershoot γ. (D) Scaled radiated energy η_R^{inf} vs average rise time to rupture duration $t^A_{\text{rise}}/T_{\text{rupt}}$. Solid black and red lines denote best linear and quadratic fits, respectively, with dashed lines and shaded regions illustrating regions within one standard deviation (fit parameter results displayed in Table S1 and equations (29)-(31)).

$$\overline{\tau}^E_{\text{ini}} = \overline{\tau}^D_{\text{rupt}} + \overline{\tau}_a + \overline{\Delta\tau}^E/2 \tag{20}$$

$$= \overline{\tau}^E_{\text{res}} + \frac{G}{\overline{\delta}_{\text{rupt}}} + \overline{\tau}_a + \overline{\Delta\tau}^E/2 \tag{21}$$

$$= \overline{\tau}^E_{\text{res}} + \frac{G + E_R/A}{\overline{\delta}_{\text{rupt}}} + \overline{\Delta\tau}^E/2 \tag{22}$$

$$= \overline{\tau}^E_{\text{res}} + \frac{\Delta W_0}{\overline{\delta}_{\text{rupt}}A} + \overline{\Delta\tau}^E/2. \tag{23}$$

The available energy per unit rupture area can be approximated as (Lambert et al., 2021b):

$$\frac{\Delta W_0}{\overline{\delta}_{\text{rupt}}A} \approx \left(\frac{1}{2} + \gamma\right)\overline{\Delta\tau}^E, \text{ where} \tag{24}$$

$$\gamma = \left(\overline{\tau}^E_{\text{fin}} - \overline{\tau}^E_{\text{res}}\right)/\overline{\Delta\tau}^E, \tag{25}$$

where γ is the scaled dynamic undershoot, which can be negative (but close to zero) for crack-like ruptures. This relation assumes that the fault resistance does not recover appreciably from the minimum level of average dynamic stress before the final slip. Note that, in the absence of any considerable dynamic overshoot or undershoot ($\gamma \approx 0$), as relevant to most crack-like ruptures, the available energy can be estimated as half of the product of the energy-based static stress drop and average slip, as traditionally done (Kanamori and Brodsky, 2004; Lambert et al., 2021b). In contrast, simulated self-healing pulses exhibit considerable dynamic undershoot (with γ up to 4), resulting in notably larger available energy than given by $\overline{\Delta\tau}^E\overline{\delta}_{\text{rupt}}/2$, as encapsulated in equation (24). Following Lambert et al. (2021b), we refer to the quantity

$\overline{\Delta\tau}^E\overline{\delta}_{\text{rupt}}/2$ as the seismologically-inferable available energy, since it can be inferred from seismological observations yet does not always represent the true available energy (Abercrombie and Rice, 2005; Rice, 2006; Ye et al., 2016; Lambert et al., 2021b).

Note that if the breakdown energy G also represents a negligible contribution to the overall earthquake energy budget (i.e. $G \approx 0$ and $\Delta W_0 \approx E_R/A\overline{\delta}_{\text{rupt}} = \overline{\tau}_a$), then the dynamic undershoot γ can be directly related to the seismically-inferable radiation ratio η_R^{inf} (which is equal to scaled radiated energy):

$$\overline{\tau}_a \approx \left(\frac{1}{2} + \gamma\right)\overline{\Delta\tau}^E, \tag{26}$$

$$\gamma \approx \frac{\eta_R^{\text{inf}}}{2} - \frac{1}{2}. \tag{27}$$

Our simulations show that a scaling relationship may indeed exist between the dynamic undershoot γ, the seismically-inferable radiation ratio η_R^{inf}, and a measure of the sharpness of the local rupture duration, such as the ratio of the rise time to rupture duration, $t_{\text{rise}}^A/T_{\text{rupt}}$ (Fig. 8; Lambert et al., 2021b). In other words, γ can be determined as:

$$\gamma = F(\eta_R, t_{\text{rise}}^A/T_{\text{rupt}}), \tag{28}$$

where $F(\eta_R, t_{\text{rise}}^A/T_{\text{rupt}})$ is a function that may in principle be determined from modeling. The modeling results of Lambert et al. (2021b) suggest that the dynamic undershoot γ and seismically-inferable radiation ratio η_R^{inf} of simulated ruptures are highly correlated with a linear correlation coefficient of 0.97. These modeling results also suggest that both γ and η_R^{inf} are anticorrelated with the logarithm of the average rise time to rupture duration $\log_{10}(t_{\text{rise}}^A/T_{\text{rupt}})$, with correlation coefficients of -0.98 and -0.96, respectively (Fig. 8). The strong correlation between these three source properties suggests that they may be reasonably related to one another linearly as (Fig. 8 and Supplementary Table S4):

$$\gamma = F_1(\eta_R^{\text{inf}}) = 0.56\eta_R^{\text{inf}} - 0.18 \tag{29}$$

$$\gamma = F_2(t_{\text{rise}}^A/T_{\text{rupt}}) = -2.29\log_{10}(t_{\text{rise}}^A/T_{\text{rupt}}) - 0.74 \tag{30}$$

$$\log_{10}(t_{\text{rise}}^A/T_{\text{rupt}}) = F_3(\eta_R^{\text{inf}}) = -0.24\eta_R^{\text{inf}} - 0.26. \tag{31}$$

More sophisticated nonlinear relations may also be determined between these source properties; however linear relations appear sufficient to fit the modeling results of Lambert et al. (2021b) based on 2-D models of single planar faults (Fig. 8 and Supplementary Table S4). Note that the linear relation between undershoot γ and radiation ratio η_R^{inf} determined from our modeling results (equation (29)) differs from the predicted trend in equation (27) in part due to the non-zero contribution of average breakdown energy to the overall energy partitioning for our simulated ruptures (Fig. 4).

Thus, for natural earthquakes, if (i) one can infer the ratio of average local rise time to rupture duration $t_{\text{rise}}^A/T_{\text{rupt}}$ and/or the seismically-inferable radiation ratio η_R^{inf}, (ii) the relation $\gamma = F(\eta_R^{inf}, t_{\text{rise}}^A/T_{\text{rupt}})$ is known (for example, from modeling), and (iii) one has insight, from numerical or lab modeling, or geological observations, into the residual stress level $\overline{\tau}_{\text{res}}^E$ which is equal to the minimal fault resistance, then the energy-based prestress can be estimated as:

$$\overline{\tau}_{\text{ini}}^E \approx \overline{\tau}_{\text{res}}^E + (1+\gamma)\,\overline{\Delta\tau}^E \tag{32}$$

$$= \overline{\tau}_{\text{res}}^E + \left[1 + F(\eta_R, t_{\text{rise}}^A/T_{\text{rupt}})\right]\overline{\Delta\tau}^E. \tag{33}$$

If the shear resistance drops to near-zero values during large earthquake ruptures and hence $\overline{\tau}_{\text{res}}^E = 0$, then the energy-averaged prestress $\overline{\tau}_{\text{ini}}^E$ can potentially be approximated purely from seismologically inferable quantities, with input from modeling to determine $F(\eta_R^{\text{inf}}, t_{\text{rise}}^A/T_{\text{rupt}})$. These results motivate more detailed study of scaling relationships among source properties of 3-D dynamic rupture scenarios, including more realistic fault geometries and various forms of fault heterogeneity.

5. Seismological observations from large earthquakes

If large earthquakes predominantly propagate as sharp self-healing pulses, as suggested by Heaton (1990), then the apparent stress from such ruptures should be notably higher than their energy-based static stress drops. This does not appear to be the case given current seismological estimates, at least for large megathrust earthquakes which make up the majority of recorded events (Ye et al., 2016; Lambert et al., 2021b). Typical values of apparent stress are 1.5 MPa for interplate strike-slip earthquakes and 0.3 MPa for megathrust earthquakes (Choy and Boatwright, 1995; Perez-Campos and Beroza, 2001; Ide and Beroza, 2001; Ye et al., 2016), with values systematically higher for strike-slip events than thrust events, by up to an order of magnitude (Choy and Boatwright, 1995; Perez-Campos and Beroza, 2001). So while the significantly higher values of apparent stress for interplate strike-slip events do suggest that these ruptures are more pulse-like, according to our modeling (Fig. 8; Lambert et al., 2021b), the current estimates of apparent stress of 0.5-2 MPa represent relatively mild additions to energy-averaged shear stress above shear heating constraints.

Note that the apparent stress estimates can be affected by a number of factors, including attenuation, rupture directivity, focal mechanism, and regional vs. teleseismic data (Perez-Campos and Beroza, 2001; Ide and Beroza, 2001; Ye et al., 2016). For example, the higher apparent stress estimates for strike-slip events are typically obtained from regional data, while the lower apparent stress estimates for megathrust events are obtained from teleseismic data. Our simulation results suggest that re-examining seismological estimates of apparent stress and energy-based static stress drop may thus provide further insight into the predominant style of rupture propagation for large earthquakes and absolute stress conditions on faults, including potential systematic differences between tectonic settings.

Yet there is some observational evidence that fault ruptures can propagate as sharp self-healing pulses and hence potentially result in much larger apparent stresses. For example, the study of Heaton (1990) considered strong ground motion recordings of local rupture duration from several large earthquakes and found that the average rise time during these events were as low as 10% of the rupture duration (Table 1). Moreover, seismological inferences based on regional data for some large crustal earthquakes, including several studied by Heaton (1990), suggest comparable or higher values of apparent stress to static stress drop, indicative of a dynamic undershoot in self-healing pulses (Table 1). We can estimate the expected undershoot and the ratio of average local rise time to rupture duration for these ruptures based on seismological inferences of static stress drop and apparent stress, using our empirical scaling (equations (29) - (31), Table 1). Such exercise suggests that some large crustal earthquakes (1971 M6.5 San Fernando, 1979 M6.5 Imperial Valley, 1979 M5.9 Coyoto Lake, 1995 Kobe, and 2000 Tottori) did propagate as self-healing pulses with potential undershoot of around 1 to 2 times their inferred static stress drop. However, the predicted undershoot for most of the other large crustal events based on existing seismological estimates show typical values between 0 to 1 (Table 1), i.e. lower than the static stress drop, which may be more consistent with crack-like

Table 1
Seismologically inferred source properties for large crustal earthquakes and predictions based on empirical scaling from numerical modeling. Radiated energy estimates are denoted as regional E_R^r or teleseismic E_R^t, where available. Moment-based stress drops $\overline{\Delta\tau}_M = CM_0/A^{3/2}$, are estimated assuming a rigidity of $\mu = 3 \times 10^{10}$ N-m^{-2}, and a rectangular source region with area A and prefactor C that depend on the rupture aspect ratio estimated from finite fault inversions as detailed in (Lambert et al., 2021b, including references for source estimates therein). Regional estimates of apparent stress $\overline{\tau}_a^r$ are calculated based on the corresponding radiated energy estimates. Inferred estimates of average dislocation rise time to rupture duration ratios $\bar{t}^A/T_{\text{rupt}}$ from strong ground motions are reported where available (Heaton, 1990). Predictions for average stress undershoot γ and rise time to rupture duration ratios $t^A_{\text{rise}}/T_{\text{rupt}}$ are calculated using regional estimates of apparent stress and static stress drops with the empirical scaling (equations (29) - (31)) derived from numerical simulations of Lambert et al. (2021b), considering one standard error range.

Earthquake	Inferred						Prediction	
	E_R^t (J)	E_R^r (J)	M_0 (N-m)	$\overline{\Delta\tau}_M$ (MPa)	$\overline{\tau}_a^r$ (MPa)	$\bar{t}^A/T_{\text{rupt}}$	$t^A_{\text{rise}}/T_{\text{rupt}}$	γ
San Fernando 1971	–	1.5e+15	7.0e+18	8.1	6.4	0.26	0.18 – 0.30	0.59 – 0.96
Coyote Lake 1979	–	4.6e+13	3.5e+17	4.1	3.9	0.35	0.15 – 0.25	0.65 – 1.1
Imperial Valley 1979	–	5.9e+14	6.7e+18	1.7	2.6	0.22	0.08 – 0.13	1.3 – 1.8
Morgan Hill 1986	–	1.4e+14	2.1e+18	2.9	2.0	0.10	0.20 – 0.34	0.36 – 0.83
Loma Prieta 1989	5.4e+14	2.7e+15	3.1e+19	4.8	2.6	–	0.23 – 0.40	0.19 – 0.67
Landers 1992	3.0e+15	1.2e+16	7.7e+19	7.6	4.7	–	0.21 – 0.36	0.28 – 0.75
Northridge 1994	3.1e+14	1.2e+15	1.3e+19	6.3	1.9	–	0.30 – 0.52	-0.08 – 0.39
Kobe 1995	8.5e+14	1.5e15	2.4e+19	1.7	1.9	–	0.12 – 0.21	0.84 – 1.3
Hector Mine 1999	2.6e+15	3.2e+15	6.3e+19	15.5	1.5	–	0.38 – 0.64	-0.31 – 0.16
Tottori 2000	1.8e+15	1.3e+15	1.2e+19	2.3	3.3	–	0.08 – 0.14	1.2 – 1.7
Denali 2002	3.6e+16	–	7.6e+20	10.4	–	–	–	–
Fukuoka 2005	–	6.5e+14	1.2e+19	3.3	1.6	–	0.25 – 0.42	0.13 – 0.60
Kumamoto 2016	–	2.1e+15	5.1e+19	9.5	1.2	–	0.37 – 0.63	-0.28 – 0.20
Izmit 1999	6.0e+15	–	2.1e20	18.6	–	–	–	–

to mildly pulse-like rupture propagation compared to some of our sharper simulated self-healing pulses with dynamic undershoot of 2 or larger (Fig. 4). The predictions based on the inferred apparent stress and static stress drop using the scaling of equations (29) - (31) do suggest that some of the earthquakes studied by Heaton (1990) may have propagated as even sharper pulses with shorter average rise times than reported (Table 1).

6. Discussion and conclusions

The average shear prestress before rupture represents a measure of the average shear stress that the fault can hold before failing in a rupture over that region, and hence serves as a measure of the *average quasi-static fault strength* over the scale of the rupture area. We propose that it is this quasi-static fault strength that is relevant to geodynamic constraints. The energy-based average prestress $\overline{\tau}^E_{\text{ini}}$ (equations (4) and (14)-(16)) may provide a more physical interpretation of the average fault strength than the spatially-averaged shear prestress τ^A_{ini}, since $\overline{\tau}^E_{\text{ini}}$ is representative of the shear resistance acting against motion, whereas τ^A_{ini} is not.

The energy-based approach to stress averaging highlights that the average measure of on-fault dynamic resistance can be thought about in two ways. First, it is reflected in the average dissipation-based shear stress, $\overline{\tau}^D_{\text{rupt}}$. That includes the resistance both from the break-down processes at and behind the rupture tip, quantified through breakdown energy (often called "fracture energy") and residual resistance of the fault $\overline{\tau}^E_{\text{res}}$. Assuming that both of these dissipative contributions are mainly converted into heat (Chester et al., 2005; Aben et al., 2019), $\overline{\tau}^D_{\text{rupt}}$ is the relevant stress measure to interpret heat-based fault stress constraints. One could also think about the average residual shear resistance $\overline{\tau}^E_{\text{res}}$ as being the appropriate measure of dynamic resistance, with $f_{\text{res}} = \overline{\tau}^E_{\text{res}}/(\sigma - p_{\text{int}})$ being similar to the notion of residual - also called dynamic - friction within slipping regions of frictional ruptures (e.g. Kanamori and Brodsky, 2004; Abercrombie and Rice, 2005; Rice, 2006; Kanamori and Rivera, 2006; Perry et al., 2020; Lambert and Lapusta, 2020; Lambert et al., 2021a). At the same time, the dissipation-based dynamic friction coefficient $f_{\text{dyn}} = \overline{\tau}^D_{\text{rupt}}/(\sigma - p_{\text{int}})$ would be more appropriate to compare with inferred values of effective friction based on thermal measurements (e.g. Brune et al., 1969; Lachenbruch and Sass, 1980; Tanikawa and Shimamoto, 2009; Fulton et al., 2013; Gao and Wang, 2014).

The energy-based prestress $\overline{\tau}^E_{\text{ini}}$ can, in principle, be inferred from field observations (equation (16)). If the dissipation-based average stress $\overline{\tau}^D_{\text{rupt}}$ can be determined from thermal constraints, then the average energy-based rupture stress $\overline{\tau}^E_{\text{rupt}}$ is that plus the apparent stress, which is in turn proportional to scaled radiated energy and static stress drop. The average fault pre-stress before an earthquake rupture is larger than the average energy-based rupture stress by a half of the energy-based stress drop (equation (15); Beeler et al., 2003).

We have re-arranged the energy balance (equation (15)) to arrive at another decomposition of the energy-based prestress that depends on the average rupture undershoot, slip, static stress drop, and residual shear resistance (equation (32)). This decomposition highlights the relation between these quantities and can be used to potentially constrain the average prestress, by estimating rupture undershoot and minimum shear resistance for different physical assumptions from numerical modeling and laboratory experiments.

We find that, in our models, the energy-based shear stress is comparable to the simple spatial average of the shear stress (Supplementary Figure S4), and hence our conclusions could be broadly transferable to that averaging if one needs to consider it. Note that, while shear stress heterogeneity spontaneously develops in our models, our seismogenic regions are homogeneous otherwise, which may affect the relation between energy-based and simple spatial averages (Noda et al., 2013), and requires further study for heterogeneous and/or rough faults.

Our SEAS simulations illustrate the difference between the dissipation-based average shear stress $\overline{\tau}^D_{\text{rupt}}$ (relevant to heat production) and the energy-based fault prestress $\overline{\tau}^E_{\text{ini}}$ (relevant to maintaining topography) depends on the mode of rupture propagation. Our simulations further demonstrate just how large this difference (related to apparent stress) can be, for plausible fault properties (Fig. 7). Rapid co-seismic weakening and healing during self-healing pulses can allow substantial motion to occur locally at low dynamic resistance, 10 MPa or less, consistent with low heat production, while larger fault areas away can maintain higher average stress levels (20-30 MPa or more). In contrast, crack-like ruptures

do not experience such rapid healing and have similar dynamic and final shear stresses, maintaining average shear stress levels within one static stress drop of the dissipation-based rupture stress (Fig. 6). In other words, simulated faults with significant co-seismic weakening and healing, and hence self-healing pulses, have a much larger difference between the energy-based prestress, a measure of fault quasi-static strength relevant for geodynamic considerations, and the dissipation-based average stress during rupture, a measure of dynamic fault resistance that would dominate heat production (Fig. 7), than chronically weak faults with crack-like ruptures. For example, for fault models with energy-based stress drops of 5 MPa, typical for natural earthquakes, and significant weakening/healing that lead to self-healing pulses with average rise times within 10% of the rupture duration, the difference can be 10-15 MPa, implying that the heat-production constraint of 10-15 MPa can correspond to average fault prestress of 20-30 MPa. For chronically weak faults with crack-like ruptures, the difference would be comparable to the average static stress drop of 5 MPa.

Coming back to the general relation (equation (16)), the difference between the geodynamic and similar estimates of average fault prestress, which reflect $\overline{\tau}^{E}_{\text{ini}}$, and fault stresses based on shear heating constraints, which quantify $\overline{\tau}^{\text{D,heat}}_{\text{rupt}}$, is due to three potential sources: the apparent stress $\overline{\tau}_a$, the resistance representing non-heat dissipating processes, $\overline{\tau}^{\text{D,other}}_{\text{rupt}}$, and half the energy-based static stress drop, $\overline{\Delta\tau}^{E}$. Given current seismic observations of about 1 MPa for apparent stress (section 5), 1-5 MPa, on average, for half of the static stress drops, and current assumptions of non-heat dissipation being negligible compared to heat production (3-10%, corresponding to less than 1 MPa given the heat constraint of 10 MPa), the discrepancy cannot be much larger than 3-7 MPa. This modest difference is consistent with those from topography and heat-based estimates for megathrusts (e.g. Gao and Wang, 2014; Dielforder et al., 2020), potentially supporting the interpretation of megathrusts as persistently weak faults that host predominantly crack-like ruptures.

However, if geodynamic considerations, such as maintaining surface topography, require that some mature plate boundary fault segments accommodate average shear stresses larger by more than 3-7 MPa than those inferred from heat flow constraints, then either (1) large earthquakes on such faults propagate predominantly as sharp self-healing pulses, with the associated apparent stress and radiated energy being currently significantly underestimated; (2) the static stress drops are substantially underestimated; and/or (3) a substantial portion of the total dissipated energy during large earthquake ruptures is consumed through processes other than heat production, notably larger than 3% or so currently considered based on existing geological and laboratory studies. Our modeling results highlight the potential for option (1) and suggest that further work to re-examine seismological estimates of radiated energy and static stress drop, as well as the relative partitioning of different sinks of dissipated energy during earthquake source processes, would provide substantial further insight into the rupture style of large earthquakes and absolute stress conditions on mature low-heat faults.

CRediT authorship contribution statement

Valère Lambert: Conceptualization, Formal analysis, Investigation, Methodology, Writing – original draft, Writing – review & editing. **Nadia Lapusta:** Conceptualization, Formal analysis, Methodology, Writing – original draft, Writing – review & editing.

Declaration of competing interest

The authors declare that they have no known competing financial interests or personal relationships that could have appeared to influence the work reported in this paper.

Data availability

Data is accessible through the Cal-716 techDATA repository (https://data.caltech.edu/records/1619 and ∼/1620).

Acknowledgements

This study was supported by the National Science Foundation (grants EAR 1142183 and 1520907) and the Southern California Earthquake Center (SCEC), contribution No. 10799. SCEC is funded by NSF Cooperative Agreement EAR-1033462 and USGS Cooperative Agreement G12AC20038. The numerical simulations for this work were done on the supercomputing cluster in the Caltech High Performance Computing Center. The data supporting the analysis and conclusions is given in Figures and Tables, in the main text and supplementary materials. Data is accessible through the CaltechDATA repository (https://data.caltech.edu/records/1619 and ∼/1620). We thank Tom Heaton, Hiroo Kanamori, Michael Gurnis, Joann Stock, Mark Simons, Jean-Philippe Avouac, Zhongwen Zhan, Rishav Mallick and Armin Dielforder for helpful discussions and review.

Appendix A. Supplementary material

Supplementary material related to this article can be found online at https://doi.org/10.1016/j.epsl.2023.118277.

References

Aben, F.M., Brantut, N., Mitchell, T.M., David, E.C., 2019. Rupture energetics in crustal rock from laboratory-scale seismic tomography. Geophys. Res. Lett. 46, 7337–7344. https://doi.org/10.1029/2019GL083040.

Abercrombie, R.E., Rice, J.R., 2005. Can observations of earthquake scaling constrain slip weakening? Geophys. J. Int. 162, 406–424. https://doi.org/10.1111/j.1365-246X.2005.02579.x.

Allmann, B.P., Shearer, P.M., 2009. Global variations of stress drop for moderate to large earthquakes. J. Geophys. Res., Solid Earth 114. https://doi.org/10.1029/2008JB005821.

Beeler, N.M., Wong, T.F., Hickman, S.H., 2003. On the expected relationships among apparent stress, static stress drop, effective shear fracture energy, and efficiency. Bull. Seismol. Soc. Am. 93, 1381–1389.

Brown, K., Kopf, A., Underwood, M., Weinberger, J., 2003. Compositional and fluid pressure controls on the state of stress on the Nankai subduction thrust: a weak plate boundary. Earth Planet. Sci. Lett. 214, 589–603.

Brune, J.N., Henyey, T.L., Roy, R.F., 1969. Heat flow, stress, and rate of slip along the San Andreas Fault, California. J. Geophys. Res. 74, 3821–3827.

Byerlee, J., 1978. Friction of rocks. Pure Appl. Geophys. 116, 615–626. https://doi.org/10.1007/BF00876528.

Chester, F.M., Chester, J.S., 1998. Ultracataclasite structure and friction processes of the Punchbowl fault, San Andreas system, California. Tectonophysics 295, 199–221. https://doi.org/10.1016/S0040-1951(98)00121-8.

Chester, J.S., Chester, F.M., Kronenberg, A.K., 2005. Fracture surface energy of the Punchbowl Fault, San Andreas system. Nature 437, 133.

Choy, G.L., Boatwright, J.L., 1995. Global patterns of radiated seismic energy and apparent stress. J. Geophys. Res., Solid Earth 100, 18205–18228. https://doi.org/10.1029/95JB01969.

Di Toro, G., Han, R., Hirose, T., De Paola, N., Nielsen, S., Mizoguchi, K., Ferri, F., Cocco, M., Shimamoto, T., 2011. Fault lubrication during earthquakes. Nature 471, 494.

Dielforder, A., 2017. Constraining the strength of megathrusts from fault geometries and application to the Alpine collision zone. Earth Planet. Sci. Lett. 474, 49–58. https://doi.org/10.1016/j.epsl.2017.06.021.

Dielforder, A., Hetzel, R., Oncken, O., 2020. Megathrust shear force controls mountain height at convergent plate margins. Nature 582, 225–229. https://doi.org/10.1038/s41586-020-2340-7.

Dieterich, J.H., 1979. Modeling of rock friction 1. Experimental results and constitutive equations. J. Geophys. Res. 84, 2161–2168.

Fay, N., Humphreys, E., 2006. Dynamics of the salton block: absolute fault strength and crust-mantle coupling in southern California. Geology 34, 261–264. https://doi.org/10.1130/G22172.1.

Fialko, Y., Rivera, L., Kanamori, H., 2005. Estimate of differential stress in the upper crust from variations in topography and strike along the San Andreas fault. Geophys. J. Int. 160, 527–532. https://doi.org/10.1111/j.1365-246X.2004.02511.x.

Fulton, P.M., Brodsky, E.E., Kano, Y., Mori, J., Chester, F., Ishikawa, T., Harris, R.N., Lin, W., Eguchi, N., Toczko, S., Expedition 343, 343T, and KR13-08 Scientists, 2013. Low coseismic friction on the Tohoku-Oki fault determined from temperature measurements. Science 342, 1214–1217. https://doi.org/10.1126/science.1243641.

Gao, X., Wang, K., 2014. Strength of stick-slip and creeping subduction megathrusts from heat flow observations. Science 345, 1038–1041. https://doi.org/10.1126/science.1255487.

Heaton, T.H., 1990. Evidence for and implications of self-healing pulses of slip in earthquake rupture. Phys. Earth Planet. Inter. 64, 1–20.

Ide, S., Beroza, G.C., 2001. Does apparent stress vary with earthquake size? Geophys. Res. Lett. 28, 3349–3352.

Kanamori, H., Brodsky, E.E., 2004. The Physics of Earthquakes. Reports on Progress in Physics, vol. 67, pp. 1429–1496.

Kanamori, H., Rivera, L., 2006. Energy partitioning during an earthquake. Am. Geophys. Union, 3–13. https://doi.org/10.1029/170GM03.

Ke, C.Y., McLaskey, G.C., Kammer, D.S., 2022. Earthquake breakdown energy scaling despite constant fracture energy. Nat. Commun. 13, 1005. https://doi.org/10.1038/s41467-022-28647-4.

Lachenbruch, A.H., Sass, J.H., 1980. Heat flow and energetics of the San Andreas Fault zone. J. Geophys. Res., Solid Earth 85, 6185–6222. https://doi.org/10.1029/JB085iB11p06185.

Lamb, S., 2006. Shear stresses on megathrusts: implications for mountain building behind subduction zones. J. Geophys. Res., Solid Earth 111. https://doi.org/10.1029/2005JB003916.

Lambert, V., Lapusta, N., 2020. Rupture-dependent breakdown energy in fault models with thermo-hydro-mechanical processes. Solid Earth 11, 2283–2302. https://doi.org/10.5194/se-11-2283-2020.

Lambert, V., Lapusta, N., Faulkner, D., 2021a. Scale dependence of earthquake rupture prestress in models with enhanced weakening: implications for event statistics and inferences of fault stress. J. Geophys. Res., Solid Earth 126, e2021JB021886. https://doi.org/10.1029/2021JB021886.

Lambert, V., Lapusta, N., Perry, S., 2021b. Propagation of large earthquakes as self-healing pulses or mild cracks. Nature 591, 252–258. https://doi.org/10.1038/s41586-021-03248-1.

Lapusta, N., Rice, J.R., Ben-Zion, Y., Zheng, G., 2000. Elastodynamic analysis for slow tectonic loading with spontaneous rupture episodes on faults with rate- and state-dependent friction. J. Geophys. Res. 105, 765–789. https://doi.org/10.1029/2000JB900250.

Lockner, D.A., Morrow, C., Moore, D., Hickman, S., 2011. Low strength of deep San Andreas fault gouge from SAFOD core. Nature 472, 82–85. https://doi.org/10.1038/nature09927.

Luttrell, K.M., Smith-Konter, B., 2017. Limits on crustal differential stress in southern California from topography and earthquake focal mechanisms. Geophys. J. Int. 211, 472–482. https://doi.org/10.1093/gji/ggx301.

Luttrell, K.M., Tong, X., Sandwell, D.T., Brooks, B.A., Bevis, M.G., 2011. Estimates of stress drop and crustal tectonic stress from the 27 February 2010 Maule, Chile, earthquake: implications for fault strength. J. Geophys. Res., Solid Earth 116. https://doi.org/10.1029/2011JB008509.

Madariaga, R., 1976. Dynamics of an expanding circular fault. Bull. Seismol. Soc. Am. 66, 639–666.

McGarr, A., 1999. On relating apparent stress to the stress causing earthquake fault slip. J. Geophys. Res., Solid Earth 104, 3003–3011.

Noda, H., Dunham, E.M., Rice, J.R., 2009. Earthquake ruptures with thermal weakening and the operation of major faults at low overall stress levels. J. Geophys. Res., Solid Earth 114. https://doi.org/10.1029/2008JB006143.

Noda, H., Lapusta, N., 2010. Three-dimensional earthquake sequence simulations with evolving temperature and pore pressure due to shear heating: effect of heterogeneous hydraulic diffusivity. J. Geophys. Res. 115, B123414. https://doi.org/10.1029/2010JB007780.

Noda, H., Lapusta, N., 2012. On averaging interface response during dynamic rupture and energy partitioning diagrams for earthquakes. J. Appl. Mech. 79. https://doi.org/10.1115/1.4005964.

Noda, H., Lapusta, N., Kanamori, H., 2013. Comparison of average stress drop measures for ruptures with heterogeneous stress change and implications for earthquake physics. Geophys. J. Int. https://doi.org/10.1093/gji/ggt074.

Palmer, A.C., Rice, J., 1973. The growth of slip surfaces in the progressive failure of over-consolidated clay. Proc. R. Soc. Lond., Ser. A, Math. Phys. Eng. Sci. 332, 527–548.

Perez-Campos, X., Beroza, G.C., 2001. An apparent mechanism dependence of radiated seismic energy. J. Geophys. Res., Solid Earth 106, 11127–11136. https://doi.org/10.1029/2000JB900455.

Perry, S.M., Lambert, V., Lapusta, N., 2020. Nearly magnitude-invariant stress drops in simulated crack-like earthquake sequences on rate-and-state faults with thermal pressurization of pore fluids. J. Geophys. Res., Solid Earth 125, e2019JB018597. https://doi.org/10.1029/2019JB018597.

Rice, J.R., 2006. Heating and weakening of faults during earthquake slip. J. Geophys. Res. 111, B05311. https://doi.org/10.1029/2005JB004006.

Ruina, A., 1983. Slip instability and state variable friction laws. J. Geophys. Res. 88, 10359–10370.

Savage, J.C., Wood, M.D., 1971. The relation between apparent stress and stress drop. Bull. Seismol. Soc. Am. 61, 1381–1388.

Shearer, P.M., Prieto, G.A., Hauksson, E., 2006. Comprehensive analysis of earthquake source spectra in southern California. J. Geophys. Res., Solid Earth 111. https://doi.org/10.1029/2005JB003979.

Sibson, R.H., 1973. Interactions between temperature and pore-fluid pressure during earthquake faulting and a mechanism for partial or total stress relief. Nature 243, 66–68.

Sibson, R.H., 1975. Generation of pseudotachylyte by ancient seismic faulting. Geophys. J. R. Astron. Soc. 43, 775–794. https://doi.org/10.1111/j.1365-246X.1975.tb06195.x.

Suppe, J., 2007. Absolute fault and crustal strength from wedge tapers. Geology 35, 1127–1130. https://doi.org/10.1130/G24053A.1.

Tanikawa, W., Shimamoto, T., 2009. Frictional and transport properties of the chelungpu fault from shallow borehole data and their correlation with seismic behavior during the 1999 Chi-Chi earthquake. J. Geophys. Res., Solid Earth 114. https://doi.org/10.1029/2008JB005750.

Townend, J., Zoback, M.D., 2000. How faulting keeps the crust strong. Geology 28, 399–402. https://doi.org/10.1130/0091-7613(2000)28<399:HFKTCS>2.0.CO;2.

Townend, J., Zoback, M.D., 2004. Regional tectonic stress near the San Andreas fault in central and southern California. Geophys. Res. Lett. 31. https://doi.org/10.1029/2003GL018918.

Tsutsumi, A., Shimamoto, T., 1997. High-velocity frictional properties of gabbro. Geophys. Res. Lett. 24, 699–702. https://doi.org/10.1029/97GL00503.

Tullis, T., 2007. Friction of rock at earthquake slip rates. Treatise Geophys. 4, 131–152. https://doi.org/10.1016/B978-044452748-6.00064-X.

Wei, M., McGuire, J.J., 2014. The Mw 6.5 offshore northern California earthquake of 10 January 2010: ordinary stress drop on a high-strength fault. Geophys. Res. Lett. 41, 6367–6373. https://doi.org/10.1002/2014GL061043.

Wibberley, C.A.J., Shimamoto, T., 2003. Internal structure and permeability of major strike-slip fault zones: the Median Tectonic Line in Mie prefecture, southwest Japan. J. Struct. Geol. 25, 59–78. https://doi.org/10.1016/S0191-8141(02)00014-7.

Wyss, M., Brune, J.N., 1968. Seismic moment, stress, and source dimensions for earthquakes in the California-Nevada region. J. Geophys. Res. (1896–1977) 73, 4681–4694. https://doi.org/10.1029/JB073i014p04681.

Ye, L., Lay, T., Kanamori, H., Rivera, L., 2016. Rupture characteristics of major and great (Mw > 7.0) megathrust earthquakes from 1990 to 2015: 1. Source parameter scaling relationships. J. Geophys. Res., Solid Earth 121, 826–844. https://doi.org/10.1002/2015JB012426.